RSC Advances

PAPER

View Article Online
View Journal | View Issue

Cite this: *RSC Adv.*, 2021, **11**, 6798

Sb nanosheet modified separator for Li–S batteries with excellent electrochemical performance†

Linchao Zeng, ‡[ab] Jianhui Zhu,‡[ac] Minsu Liu[b] and Peixin Zhang *[a]

An air-stable antimony (Sb) nanosheet modified separator (SbNs/separator) has been prepared by coating exfoliated Sb nanosheets (SbNs) successfully onto a pristine separator through a vacuum infiltration method. The as-prepared Li–S batteries using SbNs/separators exhibit much improved electrochemical performance compared to the ones using commercial separators. The coulombic efficiency (CE) of the Li–S battery using the SbNs/separator after the initial cycle is close to 100% at a current density of 0.1 A g^{-1}, and 660 mA h g^{-1} capacity retained after 100 cycles. The rate capability of Li–S battery using SbNs/separator delivers a reversible capacity of 425 mA h g^{-1} when the current density increases to 1 A g^{-1}. The improved electrochemical performance is mainly attributed to the following reasons. Firstly, the combination of physical adsorption and chemical bonding between SbNs and lithium polysulfides (LiPSs), which efficiently inhibits the shuttle phenomena of LiPSs. Secondly, the good electronic conductivity of SbNs improves the utilization of the adsorbed LiPSs, which benefits the capacity release of active materials. Lastly, the fast conversion kinetics of intermediate LiPSs caused by the catalytic effect from SbNs further suppresses the shuttle effect of LiPSs. The SbNs/separators exhibit a great potential for the future high-performance Li–S batteries.

Received 30th November 2020
Accepted 30th January 2021

DOI: 10.1039/d0ra10100a

rsc.li/rsc-advances

Introduction

In the past decades, lithium-ion batteries (LIBs) have achieved great success in portable electronics.[1–5] However, the commonly used cathode materials (such as $LiCoO_2$, $LiMn_2O_4$, $LiFePO_4$) for LIBs have reached their limits and cannot meet the needs from many applications, for example, electric vehicles (EV) and grid energy storage.[6–8] Therefore, it is important to develop new energy storage systems with significantly higher energy density. Li–S batteries have been attracting increasingly interests due to their high theoretical specific capacity of 1675 mA h g^{-1} and high energy density of 2600 W h kg^{-1}, which is nearly 10 times higher than that of the traditional LIBs.[9–13] In addition, sulfur, which is environment-friendly and of low cost, is used as the active material in Li–S batteries.[14,15] However, the practical application of Li–S batteries are still restricted by some problems, such as the low conductivity of sulfur and the shuttle effect of lithium polysulfides (LiPSs).[16–19] Many strategies have been proposed to overcome these issues, including modifying the sulfur molecule,[20,21] optimizing the pore structure of matrix materials,[22–24] and designing new electrolytes.[25–27] Unfortunately, the problems still remain for further investigations.

Another possible strategy is to use carbonaceous conductive trap layers for LiPSs, which have been proven effective to solve both problems simultaneously.[28–31] In these cases, the carbonaceous conductive interlayers adsorb the dissolved LiPSs physically and provide a transfer pathway for electrons to reactivate the adsorbed LiPSs. However, carbonaceous material can only provide weak interaction with LiPSs due to the physical adsorption mechanism, which cannot effectively inhibit the shuttle phenomena of LiPSs. The phosphorene exfoliated from black-phosphorus (BP) is considered as a promising candidate material for trap layer in LiPSs, based on its high physical and chemical adsorption ability and high electron conductivity (~300 S m^{-1}).[32,33] Consequently, the prepared Li–S battery exhibits a stable cycle performance of 780 mA h g^{-1} after 100 cycles at 0.4 A g^{-1} and an outstanding rate performance of 600 mA h g^{-1} at 3.5 A g^{-1}.[34] However, the practical applications of phosphorene is still hindered by its poor stability at ambient environment.[35] It is an urgent task to develop a suitable trap layer material that possesses simultaneously high electron conductivity, high adsorption ability for LiPSs, and high ambient stability.

Metallic antimony with gray allotrope (Sb, *R3m* space group), an element in the same group as phosphorus, is also a layered material consisting of fused, ruffled, six-membered rings, which may be promising to construct a trap layer for LiPSs. Firstly, Sb is stable in the ambient environment, which can be exfoliated

[a]*College of Chemistry and Environmental Engineering, Shenzhen University, Shenzhen 518060, P. R. China. E-mail: pxzhang@szu.edu.cn*

[b]*Shenzhen Geim Graphene Center, Tsinghua-Berkeley Shenzhen Institute, Tsinghua University, Shenzhen 518055, P. R. China*

[c]*College of Materials Science and Engineering, Xi'an University of Architecture and Technology, Xi'an, Shannxi 710055, P. R. China*

† Electronic supplementary information (ESI) available. See DOI: 10.1039/d0ra10100a

‡ Zeng L. and Zhu J. contributed equally to this work.

through the widely used sonication process for preparing SbNs efficiently.[36–38] Secondly, SbNs exhibit outstanding electron conductivity of $\sim 1.6 \times 10^4$ S m^{-1} for fast electron transfer.[39–41] Thirdly, the diffusion energy barrier for Li atom within SbNs is only ~0.48 eV, which benefits the transfer of Li^+ within SbNs material.[42] Lastly a stable chemical bonding can be formed between Sb atom and S atom, which will facilitate the adsorption of LiPSs to Sb material.[43]

In this work, we developed an-air stable SbNs-modified separator for Li–S batteries with excellent electrochemical performance. This was fulfilled by firstly fabricating SbNs by a sonication-assisted liquid exfoliation method. Modified separator (SbNs/separator) was then prepared by coating the exfoliated SbNs onto a commercial separator using the vacuum filtration method. The chemical interaction between SbNs and LiPSs was revealed. Compared with the Li–S batteries using commercial separators, the ones using as-prepared SbNs/separators exhibit superior electrochemical performance. When cycled at 0.1 A g^{-1}, the coulombic efficiency (CE) of Li–S battery using SbNs/separator after the initial cycle is close to 100% and the capacity retains 660 mA h g^{-1} after 100 cycles. The rate capability of Li–S battery using SbNs/separator is also excellent, delivering a reversible capacity of 425 mA h g^{-1} at a high current density of 1 A g^{-1}. The improved electrochemical performance is mainly attributed to the combination of physical adsorption and chemical bonding between SbNs and LiPSs that efficiently inhibits the shuttle phenomena of LiPSs. Besides, the fast conversion kinetics of intermediate LiPSs caused by the catalytic effect from SbNs further suppresses the shuttle effect of LiPSs. In addition, the as-prepared SbNs with relative good electronic conductivity facilitates the transfer of electrons to the adsorbed LiPSs. The method of modifying separator with air-stable SbNs holds a great promise for future high-performance Li–S batteries.

Experimental

Preparation of metallic SbNs

In a typical process, 1 g Sb powder (7440-69-9, Macklin) was suspended in 100 ml *N*-methyl-2-pyrrolidone (NMP, 872-50-4, Macklin) followed by probe ultrasonication (VCX500, Sonics) for 12 h in reflux device. The power output of the cell disruptor was set at 650 W. The obtained product was centrifugated under 1000 rpm centrifugation speeds for 15 min to obtain the supernate. After that, the obtained supernate was further centrifugated under 7000 rpm centrifugation speeds for 15 min to obtain the sediment. The obtained sediment was re-dispersed in a certain amount of NMP solvent under the ultrasonic process for 0.5 h and the obtained solution was calibrated for future use.

Preparation of SbNs/separator

Typically, a certain amount of the as-prepared SbNs solution was mixed with 8% polyvinylidene fluoride (PVDF). Then, the solution was infiltrated by vacuum filtration, in which a commercial Celgard separator was used as the filtration membrane. The obtained SbNs/separator was dried at 80 °C under a vacuum overnight. After that, the SbNs/separator was prepared. The SbNs/separator was cut with a diameter of 18 mm and was directly used as the separator for Li–S batteries. The mass loading of SbNs is about 0.6 mg cm^{-2}. The graphene coated separator and Sb coated separator were prepared through the same manner. The mass loading of graphene or Sb is about 0.6 mg cm^{-2}.

Preparation of sulfur working electrode

Sulfur (99.99%, Sigma-Aldrich) and SWNTs with a ratio of 7 : 3 were mixed homogeneously in a mortar. Then the mixture was sealed in a vacuum quartz tube and heated at 155 °C for 5 h (denoted as S@SWNT). The electrode with S@SWNT as active material was prepared by mixing S@SWNT powder, carbon black (MTI), and PVDF binder (Aldrich) at a mass ratio of 8 : 1 : 1 in NMP, followed by stirring for more than 6 h at room temperature to form a slurry. The prepared slurry was coated on aluminum foil and was dried at 80 °C under a vacuum overnight. The prepared electrode was cut into pellets with a diameter of 12 mm (denoted as S@SWNT electrode). The mass loading of S electrode is about 1.0 mg cm^{-2}.

Structural analysis and electrochemical measurements

The structures of the prepared samples were characterized by X-ray powder diffraction (XRD, MDTC-EQ-M21-01) and Raman tests (HORIBA LabRAM HR800). Filed-Emission Scanning Electron Microscopy (FESEM, MDTC-EQ-M18-01), transmission electron microscopy (TEM, JEOL, Tokyo, Japan), high-resolution TEM (HRTEM) and Atomic Force Microscopy (AFM) were employed to characterize the morphologies of the samples. X-ray photoelectron spectroscopy (XPS) tests were used to reveal the bonding situation between SbNs and LiPSs. The nitrogen adsorption/desorption isotherms were measured by an ASAP 2020 Accelerated Surface Area and Porosimetry instrument.

Electrochemical measurements

The S@SWNT electrode was directly used as the working electrode to perform batteries with 2032 coin cells. Li metal was used as counter and reference electrodes. The separator film used was SbNs/separator. (For comparison, coin cells assembled with commercial separator, graphene coated separator and Sb coated separator were also prepared.) The electrolyte was 1 M lithium bis(trifluoromethanesulfonyl)imide (LiTFSI) in 1 : 1 v/v 1,2-dimethoxyethane and 1,3-DOL containing $LiNO_3$ (1 wt%). The coin cells were assembled in a glove box (MBRAUN LABMASTER 130) filled with high pure Ar, where both moisture and oxygen levels were kept below 0.1 ppm. The galvanostatic charge–discharge tests were conducted at a voltage interval of 1.8–2.8 V. The specific capacity was calculated on the basis of the active S material. Cyclic voltammetry (CV) measurements were conducted at a scan rate of 0.2 mV s^{-1} on an electrochemical workstation (VMP-300, Bio-Logic). Electrochemical impedance spectrum (EIS) measurements were performed on the same electrochemical workstation in the frequency range from 100 kHz to 0.01 Hz.

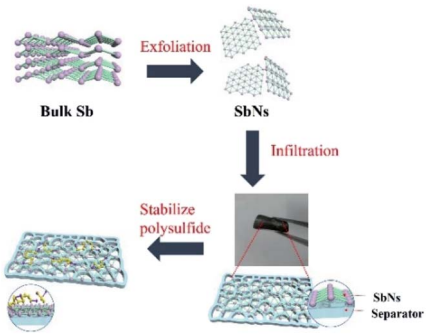

Fig. 1 Schematic illustration of the synthesis process for SbNs/separator and its mechanism in inhibiting the shuttle phenomena of polysulfide.

Results and discussion

Fig. 1 systematically illustrated the fabrication procedure of SbNs/separator and its effect in inhibiting the shuttle phenomena of LiPSs during the electrochemical cycle. Firstly, the pristine Sb powder is exfoliated into SbNs by probe ultrasonication method. Then, the SbNs/separator is prepared by vacuum filtration of the mixture of SbNs and PVDF solution using commercial separator as a filtering membrane. The prepared SbNs/separator is cut into a certain size and is directly used as the separator for Li–S batteries. During the charge–discharge process, the dissolved LiPSs are captured by SbNs and are stabilized on the surface of SbNs/separator *via* chemical adsorption and physical adsorption. As a result, the shuttle phenomena of LiPSs are effectively inhibited.

Fig. S3† shows the field-emission scanning electron microscopy (FESEM) image of pristine Sb powder. The pristine Sb powder shows a granular morphology with particle size ranging from several microns to tens of microns. Fig. 2A shows the FESEM image of the product after the probe ultrasonication process. The prepared product shows a lamellar morphology, which indicates the exfoliation phenomena of pristine Sb powder. The size of the exfoliated SbNs is about 500 nm. From the AFM image (Fig. 2B), we can see that the exfoliated SbNs shows a thickness of about 4–5 nm. Besides, the transverse size of the exfoliated SbNs is about 0.5 μm. The exfoliated sample was further characterized by transmission electron microscopy (TEM) and high-resolution transmission electron microscopy. The SbNs shows a very thin structure with a transverse size of about 0.5 μm (Fig. 2C), which is consistent with the FESEM and AFM results. From HRTEM image, the lattice fringes of the dominated (012) crystal plane of Sb with a *d*-spacing of 0.318 nm and the (006) crystal plane of Sb with a *d*-spacing of 0.200 nm can be seen clearly, which demonstrates the gray allotrope phase of Sb with a space group of *R*3*m* is not changed after exfoliation (Fig. 2D).

Fig. 2E presents the XRD patterns of pristine Sb powder and SbNs. The pristine powder shows the standard Bragg diffraction peaks of gray Sb. After the exfoliation process, the diffraction peaks of SbNs remain in the same position, but the intensity of these peaks are decreased, especially for the peak of (003) crystal plane. The decreased intensity of the diffraction peaks of SbNs

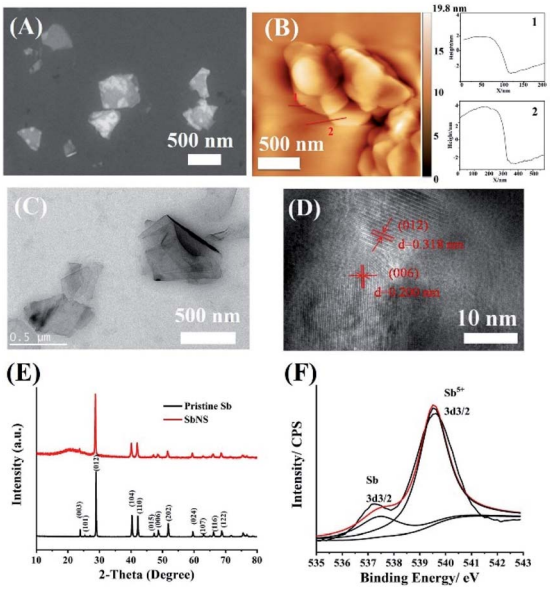

Fig. 2 FESEM (A) and AFM (B) images of SbNs. TEM (C) and HRTEM (D) images of SbNs. (E) XRD patterns of the pristine Sb powder and the SbNs powder. (F) Sb 3d high-resolution XPS spectra of SbNs.

is due to a much thinner thickness of the SbNs compared with the pristine Sb powder, which indicates an exfoliation process occurred during the probe sonication process.[36,44] Besides, no additional XRD diffraction peaks are existed in the exfoliated sample, indicating no side reaction has occurred during the probe ultrasonication process, which is consistent with the result of HRTEM. Fig. S4† shows the Raman spectra of the samples. It can be seen that the pristine powder exhibits the standard Raman characteristic peaks of Sb. After probe ultrasonication, the Raman peaks of SbNs remain at the same position with the intensity of these characteristic peaks becomes much weaker, further indicating the successful exfoliation of metallic Sb nanosheets. Fig. S5† shows the XPS of pristine Sb powder and SbNs. The XPS spectra disclosed the existence of the Sb element without any impurity in Sb powder and SbNs, indicating no side reactions occurred during the exfoliation process. Fig. 2F shows the Sb 3d high-resolution XPS spectra of SbNs. The high-resolution Sb 3d peaks can be further deconvoluted into two symmetric signals with binding energies of 540.2 and 537.8 eV that correspond to Sb $3d_{3/2}$ main peak and $3d_{3/2}$ satellite peak, respectively. The specific surface area of the pristine Sb powder and SbNs were analyzed by nitrogen Brunauer–Emmett–Teller (BET) adsorption measurements (Fig. S6†). The pristine Sb possesses a specific surface area of 0.19 $m^2\ g^{-1}$. After the exfoliation process, the BET surface area of SbNs increased sharply to 11.19 $m^2\ g^{-1}$, which is about 59 times higher than that of the pristine Sb powder. This change is ascribed to the larger surface area of 2D structured after the exfoliation process.

Fig. 3A shows the initial several cyclic voltammetry (CV) curves of Li–S battery using SbNs/separator in the potential range of 1.8–2.8 V. It exhibits two cathodic peaks (one at 2.27 V and the other at 1.94 V) in the 1st cathodic scan. The cathodic peaks at 2.27 V corresponds to the change from S to soluble

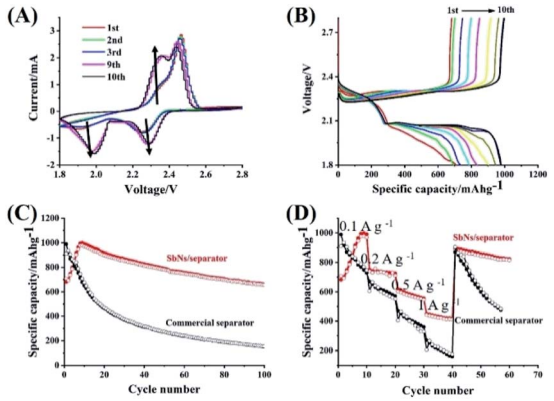

Fig. 3 (A) Initial several cyclic voltammetry (CV) curves of Li–S battery using SbNs separator in the potential range of 1.8–2.8 V. (B) Inital ten charge/discharge profiles of Li–S battery using SbNs/separator at a current density of 0.1 A g^{-1}. (C) Comparison of the charge–discharge capacities of Li–S batteries using SbNs/separator and commercial separator at a current density of 0.1 A g^{-1}. (D) Rate capabilities of Li–S battery using SbNs/separator and pristine separator.

high-order LiPSs (Li_2S_x, $4 \leq x \leq 8$) and the cathodic peaks at 1.94 V is ascribed to the change from soluble high-order LiPSs to insoluble low-order LiPSs (Li_2S_2 or Li_2S).[34] And two anodic peaks can also be seen in the 1st anodic scan, which is associated with the phase change from Li_2S to LiPSs, and then to S.[16] The current intensity of these peaks becomes much stronger after the initial cycle. This phenomena may be caused by the activation process of battery. Fig. 3B displays the initial ten charges/discharge profiles of Li–S battery using SbNs/separator at a current density of 0.1 A g^{-1}. The first discharge curve shows two high voltage plateaus (one at 2.35 V and the other at 2.0 V). The initial discharge and charge capacities of Li–S battery using SbNs/separator are 707.5 mA h g^{-1} and 681.9 mA h g^{-1}, respectively, corresponding to an initial coulombic efficiency (ICE) of 96.3%. After the initial cycle, the capacity increases gradually and reaches a highest value of 997.7 mA h g^{-1} at 9th cycle. This phenomena further confirms an activation process is involved in the battery. During the initial several cycles, the active materials are not fully activated due to some reasons, such as the restricted contacting with Li^+ or electrons. After the active materials are fully activated, the charge–discharge capacities reach highest values.[20,45]

The comparison of the charge–discharge capacities of Li–S batteries using SbNs/separator and commercial separator at a current density of 0.1 A g^{-1} is also shown in Fig. 3C. For Li–S battery using SbNs/separator, a reversible capacity of 660.8 mA h g^{-1} is maintained after 100 cycles. Besides, the CE of Li–S batteries using SbNs/separator always approaches 100% after the initial cycle, which indicates an effective role of SbNs that plays in alleviating the shuttle effect of LiPSs.[34] In the case of Li–S battery using a pristine separator, only a reversible capacity of 154 mA h g^{-1} is delivered after 100 cycles. It should be noted that Sb material contributes little capacity during the charge–discharge process, which can even be ignored (Fig. S7A†). Besides, the chemical valences of the Sb after electrochemical cycling remains unchanged, indicating its chemical stability in Li–S batteries (Fig. S8†). Fig. 3D further compares the rate capabilities of Li–S batteries using SbNs/separator and commercial separator. For Li–S batteries using SbNs/separator, it can deliver a reversible capacity as high as 920, 743, 579, and 423 mA h g^{-1}, respectively, when cycled at 0.1, 0.2, 0.5, and 1 A g^{-1}. When the current density was recovered to 0.1 A g^{-1}, the reversible capacity recovers to 878 mA h g^{-1}, indicating excellent electrochemical stability of the electrode. While for Li–S battery using a commercial separator, it exhibits a much worse rate capability compared to Li–S batteries using SbNs/separator. Only a reversible capacity of 221 mA h g^{-1} is obtained when cycled at 1 A g^{-1}. To reveal the advantages of SbNs/separator to that of graphene/separator and Sb/separator, the cycling performance of Li–S batteries using Sb/separator and graphene/separator are tested. Fig. S9† shows the nitrogen Brunauer–Emmett–Teller (BET) adsorption measurement of the graphene. The BET surface of the graphene is about 390 m^2 g^{-1}. For Li–S batteries using graphene/separator, the initial discharge and charge capacities are 863.8 mA h g^{-1} and 993.5 mA h g^{-1}, respectively (Fig. S10†). After 100 cycles, a reversible capacity of 353 mA h g^{-1} is maintained. For Li–S batteries using Sb/separator, the initial discharge and charge capacities are 760.3 mA h g^{-1} and 737.4 mA h g^{-1}, respectively (Fig. S11†). After the initial cycles, the capacity increases gradually and reaches the highest value of 958.6 mA h g^{-1} at the 5th cycle. A reversible capacity of 320 mA h g^{-1} is maintained after 100 cycles. Obviously, the cycling performance of Li–S batteries using graphene/separator and Sb/separator are improved compared with Li–S batteries using a pristine separator. However, the cycling performance of Li–S batteries using graphene/separator and Sb/separator are still much worse than Li–S batteries using SbNs/separator. This is due to the combined physical and chemical absorption of LiPSs between LiPSs and SbNs, which maximum inhibits the shuttle phenomena of LiPSs. The polarization voltages of Li–S batteries using SbNs/separator, graphene/separator, and pristine separator are shown in Fig. S12.† It can be seen that the polarization voltage of Li–S batteries using SbNs/separator ($\Delta E = 0.159$ V) is much lower than Li–S batteries using commercial separator (0.236 V) and graphene/separator (0.203 V), indicating SbNs/separator acts a positive catalyst role in facilitating the conversion of LiPSs.[46,47]

Electrochemical impedance spectrum of symmetric batteries with Li foil and commercial separator (or SbNs/separator) were tested (Fig. S13†). The R_f of symmetric battery with Li foil and SbNs/separator is a little larger than that of symmetric battery with Li foil and commercial separator, indicating the electrochemical impedance value of SbNs/separator is a little larger than that of commercial separator. Fig. S14† shows typical Nyquist plots of Li–S batteries using SbNs/separator (or commercial separator, discharged to 1.8 V after 10 cycles at a current density of 0.1 A g^{-1}). Obviously, the charge transfer impedance of Li–S batteries using SbNs/separator is much smaller than that of Li–S batteries using a commercial separator. This is due to the good conductivity of metallic SbNs that facilitates the electron transfer to the adsorbed LiPSs and the catalyst role of SbNs in facilitating the conversion of LiPSs that avoids the accumulation of nonconductive Li_2S.[48–50] To confirm

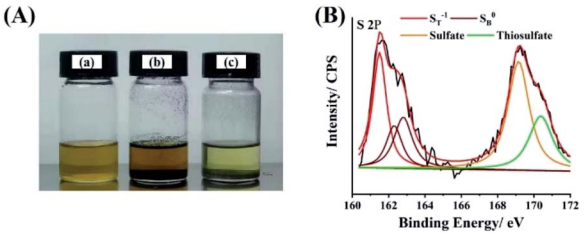

Fig. 4 (A) Digital image of the Li_2S_6 (0.005 mol L^{-1}) in DOL/DME solution: (a) control; adsorption by (b) graphene and (c) SbNs. (B) S 2p high-resolution XPS spectra of SbNs–Li_2S_6 composite.

the positive effect of SbNs in adsorbing LiPSs, graphene and SbNs with the same total surface area were immersed in DOL/DME (1 : 1, v/v) solution containing 0.005 mol L^{-1} Li_2S_6 as absorbents for one night. We can see that the SbNs exhibits much stronger polysulfide adsorption compared with that of graphene. The color of Li_2S_6 changed a lot in the solution using SbNs as absorbent (Fig. 4A). However, the color of Li_2S_6 has almost no change in the solution using graphene as absorbent, which demonstrates weak polysulfide adsorption of graphene. To further provide evidence of the chemical adsorption between LiPSs and SbNs, the XPS of SbNs that immersed in DOL/DME (1 : 1, v/v) solution containing 0.005 mol L^{-1} Li_2S_6 for one night was examined (Fig. 4B). As known, the pristine Li_2S_6 exhibits two pairs of typical peaks located at 161.3 and 163.8 eV, which ascribe to the terminal (ST^{-1}) and bridging (SB^0) sulfur, respectively. However, the peak of ST^{-1} shift to a high BE range in SbNs–Li_2S_6 composite, indicating a reduction in electron cloud density of sulfur atoms due to the chemical adsorption by SbNs.[51] Besides, the peaks at 169.2 eV and 170.4 eV are assigned to sulfate and thiosulfate, respectively, which also indicates the chemical interactions between SbNs and Li_2S_6.[51] The chemical adsorption of Li_2S_6 by SbNs is further supported by the Li 1s spectra of SbNs–Li_2S_6 composite (Fig. S15†). It has been revealed that the pristine Li_2S_6 displays a typical peak at 55.3 eV, corresponding to the Li–S bond. However, the Li–S bond shift to a lower bond of 54.9 eV. It suggests that a "lithium-bond" like configuration forms bridge the SbNs absorber and LiPSs.[51]

Based on the above discussion, the improved electrochemical performance of Li–S batteries using SbNs/separator is due to the following reasons: firstly, the combined physical and chemical absorption of LiPSs between LiPSs and SbNs efficiently inhibits the shuttle phenomena of LiPSs, which benefit the cycle stability of Li–S batteries. Secondly, the good electronic conductivity of SbNs facilitates the transfer of electrons to active material, which improves the rate performance of Li–S batteries. Besides, the catalytic effect from SbNs facilitates the fast conversion kinetics of intermediate LiPSs, which further suppresses the shuttle effect of LiPSs.

Conclusions

In summary, the air-stable SbNs/separator was successfully prepared by a two-step method. First, the pristine Sb powder was exfoliated into SbNs by probe ultrasonication process. Then, the as-prepared SbNs solution was coated onto commercial separator by the vacuum filtration method. When used as a separator material for Li–S batteries, the prepared Li–S battery exhibits better electrochemical performance compared to Li–S battery using a commercial separator. When cycled at 0.1 A g^{-1}, the coulombic efficiency (CE) of Li–S battery using SbNs/separator after the initial cycle is close to 100% and a high capacity of 660 mA h g^{-1} is maintained after 100 cycles. The rate capability of Li–S battery using SbNs/separator is also excellent. It delivers a reversible capacity of 425 mA h g^{-1} at 1 A g^{-1}. The improved electrochemical performance is attributed to the combined chemical absorption and chemical absorption between SbNs and LiPSs that efficiently inhibit the shuttle phenomena. Besides, the catalytic effect from SbNs facilitates the fast conversion kinetics of intermediate LiPSs, which further suppresses the shuttle effect of LiPSs. In addition, the good electronic conductivity of SbNs facilitates the transfer of electrons to active material, which improves the rate performance of the Li–S battery. The method of modifying separator with an air-stable and easy production material holds great promising for high-performance Li–S batteries.

Author information

The authors declare no competing financial conflicts. All authors contributed to the preparation of this manuscript. Zeng L. conducted the experiments and wrote the paper. Liu M. and Zhu J. helped with discussion and explanation of results. Zhang P. conceived the idea.

Conflicts of interest

The authors declare no competing financial conflicts.

Acknowledgements

Zeng L. and Zhu J. contributed equally to this work. This work was supported by China Postdoctoral Science Foundation (No. 2018M631462), Shenzhen Government's Plan of Science and Technology (JCYJ20170818094047620), the National Natural Science Foundation of China (51774203).

Notes and references

1 J.-Y. Hwang, S.-T. Myung and Y.-K. Sun, *Chem. Soc. Rev.*, 2017, **46**, 3529–3614.
2 D. Lin, Y. Liu and Y. Cui, *Nat. Nanotechnol.*, 2017, **12**, 194–206.
3 J. Choi and D. Aurbach, *Nat. Rev. Mater.*, 2016, **1**, 16013.
4 X. Cheng, R. Zhang, C. Zhao and Q. Zhang, *Chem. Rev.*, 2017, **117**, 10403–10473.
5 J. Tarascon and M. Armand, *Nature*, 2001, **414**, 359–367.
6 N. Nitta, F. Wu, J. Lee and G. Yushin, *Mater. Today*, 2015, **18**, 252–264.
7 A. Ramanujapuram, D. Gordon, A. Magasinski, B. Ward, N. Nitta, C. Huang and G. Yushin, *Energy Environ. Sci.*, 2016, **9**, 1841–1848.

8 Y. Mao, S. Xiao and J. Liu, *Mater. Res. Bull.*, 2017, **96**, 437–442.
9 Y. Liu, W. Kou, X. Li, C. Huang, R. Shui and G. He, *Small*, 2019, **15**, 1902431.
10 M. Li, R. Carter, A. Douglas, L. Oakes and C. Pint, *ACS Nano*, 2017, **11**, 4877–4884.
11 X. Li and X. Sun, *Adv. Funct. Mater.*, 2018, **28**, 1801323.
12 R. Fang, S. Zhao, Z. Sun, W. Wang, H. Cheng and F. Li, *Adv. Mater.*, 2017, **29**, 1606823.
13 P. Dirlam, R. Glass, K. Char and J. Pyun, *J. Polym. Sci., Part A: Polym. Chem.*, 2017, **55**, 1635–1668.
14 Y. Song, W. Cai, L. Kong, J. Cai, Q. Zhang and J. Sun, *Adv. Energy Mater.*, 2019, **10**, 1901075.
15 Q. Dong, R. Shen, C. Li, R. Gan, X. Ma, J. Wang, J. Li and Z. Wei, *Small*, 2018, **14**, 1804277.
16 M. Shaibani, A. Akbari, P. Sheath, C. Easton, P. Banerjee, K. Konstas, A. Fakhfouri, M. Barghanadi, M. Musameh, A. Best, T. Ruther, P. Mahon, M. Hill, A. Hollenkamp and M. Majumder, *ACS Nano*, 2016, **10**, 7768–7779.
17 L. Borchardt, M. Oschatz and S. Kaskel, *Chem.–Eur. J.*, 2016, **22**, 7324–7351.
18 A. Manthiram, Y. Fu, S.-H. Chung, C. Zu and Y. Su, *Chem. Rev.*, 2014, **114**, 11751–11787.
19 A. Manthiram, S.-H. Chung and C. Zu, *Adv. Mater.*, 2015, **27**, 1980–2006.
20 L. Zeng, Y. Yao, J. Shi, Y. Jiang, W. Li, L. Gu and Y. Yu, *Energy Storage Materials*, 2016, **5**, 50–57.
21 X. Li, J. Liang, K. Zhang, Z. Hou, W. Zhang, Y. Zhu and Y. Qian, *Energy Environ. Sci.*, 2015, **8**, 3181–3186.
22 Y. Chen, W. Zhang, D. Zhou, H. Tian, D. Su, C. Wang, D. Stockdale, F. Kang, B. Li and G. Wang, *ACS Nano*, 2019, **13**, 4731–4741.
23 S. Feng, J. Song, C. Zhu, Q. Shi, D. Liu, J. Li, D. Du, Q. Zhang and Y. Lin, *ACS Appl. Mater. Interfaces*, 2019, **11**, 5911–5918.
24 J. Song, Z. Yu, M. Gordin and D. Wang, *Nano Lett.*, 2016, **16**, 864–870.
25 Q. Pang, A. Shyamsunder, B. Narayanan, C. Kwok, L. Curtiss and L. Nazar, *Nat. Energy*, 2018, **3**, 783–791.
26 X. Li, D. Wang, H. Wang, H. Yan, Z. Gong and Y. Yang, *ACS Appl. Mater. Interfaces*, 2019, **11**, 22745–22753.
27 J. Zheng, G. Ji, X. Fan, J. Chen, Q. Li, H. Wang, Y. Yang, K. DeMella, S. Raghvan and C. Wang, *Adv. Energy Mater.*, 2019, **9**, 1803774.
28 J. Hwang, H. Kim, S. Shin and Y. Sun, *Adv. Funct. Mater.*, 2018, **28**, 1704294.
29 G. Zhou, L. Li, D. Wang, X. Shan, S. Pei, F. Li and H. Cheng, *Adv. Mater.*, 2015, **27**, 641–647.
30 H. Wu, Y. Huang, W. Zhang, X. Sun, Y. Yang, L. Wang and M. Zong, *J. Alloys Compd.*, 2017, **708**, 743–750.
31 Z. Du, C. Guo, L. Wang, A. Hu, S. Jin, T. Zhang, H. Jin, Z. Qi, S. Xin, X. Kong, Y. Guo, H. Ji and L. Wan, *ACS Appl. Mater. Interfaces*, 2017, **9**, 43696–43703.
32 J. Zhao, Y. Yang, R. Katiyar and Z. Chen, *J. Mater. Chem. A*, 2016, **4**, 6124–6130.
33 L. Li, L. Chen, S. Mukherjee, J. Gao, H. Sun, Z. Liu, X. Ma, T. Gupta, C. Singh, W. Ren, H. Cheng and N. Koratkar, *Adv. Mater.*, 2017, **29**, 1602734.
34 J. Sun, Y. Sun, M. Pasta, G. Zhou, Y. Li, W. Liu, F. Xiong and Y. Cui, *Adv. Mater.*, 2016, **28**, 9797–9803.
35 F. Li and J. Zhao, *ACS Appl. Mater. Interfaces*, 2017, **9**, 42836–42844.
36 J. Gu, Z. Du, C. Zhang, J. Ma, B. Li and S. Yang, *Adv. Energy Mater.*, 2017, **7**, 1700447.
37 P. Ares, F. Aguilar-Galindo, D. Rodriguez-San-Miguel, D. Aldave, S. Diaz-Tendero, M. Alcami, F. Martin, J. Gomez-Herrero and F. Zamora, *Adv. Mater.*, 2016, **28**, 6332–6336.
38 R. Gusmao, Z. Sofer, D. Bousa and M. Pumera, *Angew. Chem., Int. Ed.*, 2017, **56**, 14417–14422.
39 O. Ruiz, M. Cochrane, M. Li, Y. Yan, K. Ma, J. Fu, Z. Wang, S. Tolbert, V. Shenoy and E. Detsi, *Adv. Energy Mater.*, 2018, **8**, 1801781.
40 Y. An, Y. Tian, L. Ci, S. Xiong, J. Feng and Y. Qian, *ACS Nano*, 2018, **12**, 12932–12940.
41 P. Ares, J. Jose Palacios, G. Abellan, J. Gomez-Herrero and F. Zamora, *Adv. Mater.*, 2018, **30**, 1703771.
42 X. Wang, C. Tang, X. Zhou, W. Zhu and L. Fu, *Appl. Surf. Sci.*, 2019, **495**, 143549.
43 Z. Li, G. Xia, B. Wu, W. Huang and Z. Cheng, *J. Appl. Phys.*, 2003, **94**, 1295–1297.
44 X. Cai, Y. Luo, B. Liu and H. Cheng, *Chem. Soc. Rev.*, 2018, **47**, 6224–6266.
45 W. Li, M. Li, M. Wang, L. Zeng and Y. Yu, *Nano Energy*, 2015, **13**, 693–701.
46 T. Zhou, W. Lv, J. Li, G. Zhou, Y. Zhao, S. Fan, B. Liu, B. Li, F. Kang and Q. Yang, *Energy Environ. Sci.*, 2017, **10**, 1694.
47 Z. Hao, L. Yuan, C. Chen, J. Xiang, Y. Li, Z. Huang, P. Hu and Y. Huang, *J. Mater. Chem. A*, 2016, **4**, 17711.
48 B. Zhang, T. Sheng, Y. Liu, Y. Wang, L. Zhang, W. Lai, L. Wang, J. Yang, Q. Gu, S. Chou, H. Liu and S. Dou, *Nat. Commun.*, 2018, **9**, 4082.
49 H. Ye, J. Sun, S. Zhang, H. Lin, T. Zhang, Q. Yao and J. Lee, *ACS Nano*, 2019, **13**, 14208–14216.
50 Z. Yan, J. Xiao, W. Lai, L. Wang, F. Gebert, Y. Wang, Q. Gu, H. Liu, S. Chou, H. Liu and S. Dou, *Nat. Commun.*, 2019, **10**, 4793.
51 Y. Tian, G. Li, Y. Zhang, D. Luo, X. Wang, Y. Zhao, H. Liu, P. Ji, X. Du, J. Li and Z. Chen, *Adv. Mater.*, 2020, **32**, e1904876.